JTTEE5 13:526-536
DOI: 10.1361/10599630421442
1059-9630/$19.00 © ASM International

Peer Reviewed

Long-Term Carbide Development in High-Velocity Oxygen Fuel/High-Velocity Air Fuel Cr_3C_2-NiCr Coatings Heat Treated at 900 °C

S. Matthews, M. Hyland, and B. James

(Submitted February 10, 2003; in revised form May 12, 2003)

During the deposition of Cr_3C_2-NiCr coatings, compositional degradation occurs, primarily through the dissolution of the carbide phase into the matrix. Exposure at an elevated temperature leads to transformations in the compositional distribution and microstructure. While these have been investigated in short-term trials, no systematic investigations of the long-term microstructural development have been presented for high-velocity sprayed coatings. In this work, high-velocity air fuel (HVAF) and high-velocity oxygen fuel (HVOF) coatings were treated at 900 °C for up to 60 days. Rapid refinement of the supersaturated matrix phase occurred, with the degree of matrix phase alloying continuing to decrease over the following 20 to 40 days. Carbide nucleation in the HVAF coatings occurred preferentially on the retained carbide grains, while that in the HVOF coatings developed in the regions of greatest carbide dissolution. This difference resulted in a variation in carbide morphologies. Preferential horizontal growth was evident in both coatings over the first 20 to 30 days of exposure, beyond which spheroidization of the microstructure occurred. After 30 days, the carbide morphology of both coatings was comparable, tending toward an expansive structure of coalesced carbide grains. The development of the carbide phase played a significant role in the microhardness variation of these coatings with time.

Keywords chromium carbide, heat treatment, high-velocity air fuel, high-velocity oxygen fuel, microhardness

1. Introduction

Thermally sprayed Cr_3C_2-NiCr cermets have been used extensively to mitigate wear and erosion at high temperatures at which WC-based composites are not suitable (Ref 1, 2). During thermal spraying, substantial variations in the cermet composition and microstructure are possible as a result of exposure to the high-temperature accelerating gas (Ref 3-7). This is expected to have a significant impact on the mechanical and oxidation properties of the coating.

When dissolution of the carbide phase into the alloy matrix occurs, there is a reduction in the carbide concentration that generates marked variability in the matrix phase. Supersaturation of the matrix then occurs, resulting in a range of alloy compositions from those that are rich in chromium through to the original nickel-base alloy (Ref 6, 7). Dissolved carbon may be lost as CO or CO_2, altering the local composition and enhancing the formation of the degradation phases Cr_7C_3 and $Cr_{23}C_6$. Oxide formation can occur around the particle periphery in-flight and may potentially be distributed within the body of the particle should significant melting of the matrix occur (Ref 8).

S. Matthews, M. Hyland, and **B. James,** Department of Chemical and Materials Engineering, The University of Auckland, Auckland, New Zealand. Contact e-mail: m.hyland@auckland.ac.nz.

This widespread compositional disorder is trapped within the metastable structure as a result of rapid solidification upon deposition. In addition, the microstructure of the supersaturated matrix phase varies with the spray conditions, potentially ranging from zones of amorphous material (Ref 7, 9, 10) to the nano (Ref 9, 10) and microcrystalline phases (Ref 6).

The complex, metastable state of the as-sprayed coating means there is a large driving force for microstructural and compositional transformation at elevated temperatures. This microstructural refinement was investigated by several authors (Ref 1-6, 9-12) using short-term heat treatments, typically for periods of less than 24 h. A rapid reduction in the supersaturation of the matrix phase occurs. This typically corresponds with the precipitation of particulate phases, which are generally thought to be carbides (Ref 3-7).

The use of these coatings on turbine components (Ref 1, 3, 13), and in fluidized bed combustors (Ref 14, 15) means that they are exposed to elevated temperatures for many thousands of hours (Ref 13). Knowledge of the long-term microstructural transformations in relation to the wear and corrosion performance of these coatings is of critical importance. Aside from limited works on the variations in microhardness (Ref 1, 2, 16) and residual stress (Ref 16), the response of the coating in the long term is largely unknown. This is particularly so in the application of high-velocity thermal spray coatings. No long-term systematic studies of the microstructural evolution of these materials at high temperatures have been found. In this work, the responses of high-velocity air fuel (HVAF) and high-velocity oxygen fuel (HVOF) Cr_3C_2-NiCr coatings were assessed after exposure at 900 °C in air and argon for periods of up to 60 days.

The aim of this investigation was to identify the variation in coating composition and to quantify the development of the carbide structure as a function of time at temperature as a preliminary step to investigating the erosion resistance of heat-treated coatings.

2. Experimental Procedure

A cermet powder with a nominal composition of $75Cr_3C_2$-25NiCr (2075NiCr, WOKA, Barchfeld, Germany) was sprayed onto mild steel substrates using Aerospray HVAF (Enfield, NH) and GMA (Esneux, Belgium) Microjet HVOF thermal spray systems. Coating-only samples were prepared by cutting through the coating/substrate interface with a metallographic cutting machine. The thin layer of remaining substrate material was removed by heating in a 10% nitric acid solution. Copper plates were placed in contact with the samples to accelerate iron dissolution. The coating-only samples then were ground and polished. Analysis by x-ray diffraction (XRD) and energy dispersive x-ray spectroscopy (EDS) indicated no detectable variation in composition as a result of acid treatment. The sample dimensions after polishing were 15 × 7 mm, with the thickness of the HVAF coupons ranging from 650 to 850 μm, and that of the HVOF samples ranging from 200 to 300 μm.

2.1 Heat Treatment

Heat treatment was conducted at 900 °C in air and under a positive pressure of argon. Samples were removed after 2, 5, 10, 20, 30, 40, and 60 days. In all cases, a tarnish layer had formed and was removed by grinding, exposing the underlying heat-treated material that was not influenced by the mild oxidation that had occurred. Compositional analysis was performed using XRD (D8 Advance, Bruker, Karlsruhe, Germany; copper source at 40 mA and 40 kV). Analysis of the mounted and polished cross sections was carried out using a back-scattered electron (BSE) scanning electron microscope (XL30S FEG, Philips, Amsterdam, The Netherlands). Vickers microhardness measurements (M-400 Hardness Tester, LECO, Stockport, U.K.) were conducted on the coating cross sections under a load of 300 g for 5 s. An average hardness was calculated from 10 indents per specimen.

2.2 Characterization

Equilibrium compositions were calculated using a software package (HSC Chemistry, Outokumpo, Oy, Finland) (Ref 17). Component concentrations as a function of temperature were predicted using a Gibbs energy-minimization model based on the specified starting composition.

Characterization of the carbide development was carried out on the BSE images at a magnification of 8000×. The overall carbide volume fraction was determined by analysis of the high-magnification images using a software package (UTHSCSA Image Tool, University of Texas Health Research Center, San Antonio, TX) (Ref 18). The principle of such a method is that the area fraction of a phase in a representative cross-sectional image is equivalent to the volume fraction of that phase in the material (Ref 19, 20). Three images per sample were characterized. Only the carbide content was assessed, with any porosity, pullouts, or oxide included in the matrix content. An indicative measure of the carbide grain size and matrix free length was assessed using the linear intercept method (Ref 19-21). Due to the complex carbide morphologies encountered, particularly in the HVOF coating, the linear intercept analysis was conducted in two perpendicular directions (Fig. 1). Six lines in each direction were assessed per sample, and their combined average values were used to generate overall trends. Due to the complex microstructure, particularly over extended periods of exposure, the intercept values presented are only loosely related to the diameter of the carbide grains. They cannot be treated as spheres of equivalent diameter. As such, these values are referred to as carbide intercept lengths.

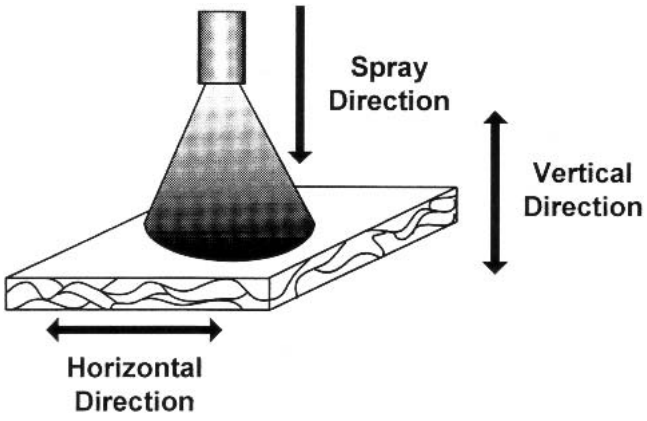

Fig. 1 Schematic illustrating the horizontal and vertical directions of the line intercept analysis of the microstructure in relation to the spray direction

3. Results and Discussion

3.1 As-Sprayed Coatings

HVOF-sprayed Cr_3C_2-NiCr coatings have been extensively investigated (Ref 3-7, 9, 10, 12). The properties and appearances of the coatings in this work are within the range previously published. Structurally, the coating splats were readily evident through the presence of oxide stringers and the variation in BSE contrast of the neighboring particles. The long, thin splat morphologies indicated that the majority of the powder particles were molten at impact. Extensive carbide dissolution occurred, resulting in widespread grayscale variation relative to the starting powder (Fig. 2). The carbide concentration was significantly reduced, with the carbide grains present predominantly in the center of the larger splats. Cr_3C_2 and NiCr were the only compounds identified in the XRD spectra (Fig. 3). While Cr_7C_3 may have formed, the concentration of this phase was not sufficient to be definitively isolated from the other peaks. The distortion of the matrix phase by carbide dissolution was reflected in the NiCr spectra (Fig. 3), with the peaks of this phase all showing higher *d*-spacing amorphous "humps," which are typical of HVOF coatings on this material (Ref 3-7, 12). While fine grained or amorphous material may have contributed to the formation of such features, they were predominantly the result of the supersaturation of the alloy with dissolved chromium and carbon.

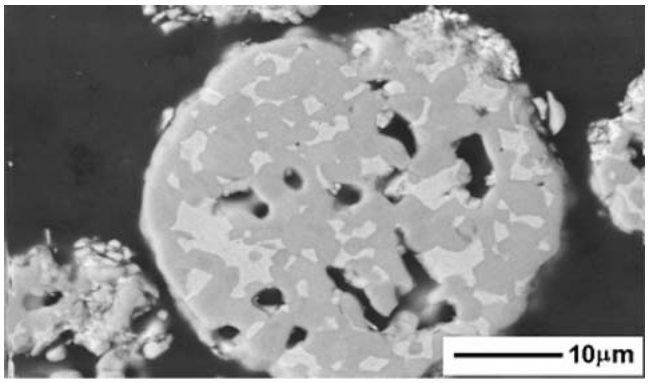

(a)

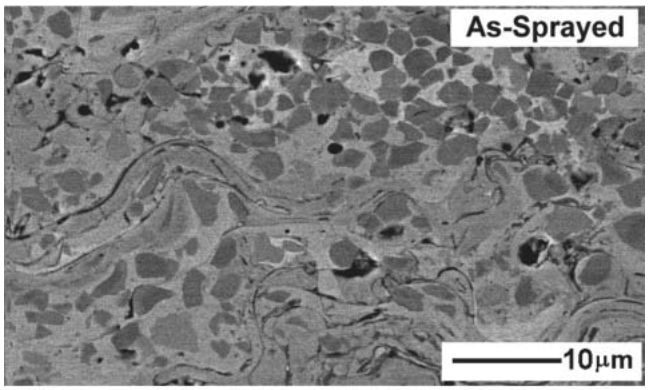

(b)

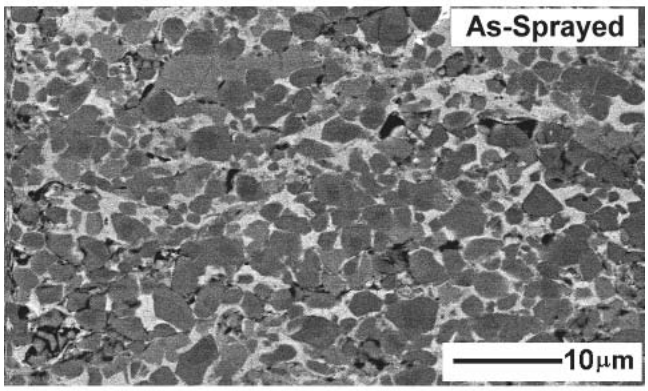

(c)

Fig. 2 BSE cross section of (a) WOKA 2075NiCr powder particle, (b) as-sprayed HVOF, and (c) as-sprayed HVAF, coatings

In marked contrast, the HVAF coating retained a high carbide concentration, with the isolated carbide grains being homogeneously distributed (Fig. 2). While few studies have been published of HVAF Cr_3C_2-NiCr coatings, these general features (low degrees of carbide degradation and homogeneous phase distribution) are consistent with the structure of HVAF WC-Co and WCCoCr coatings (Ref 22-24). Only Cr_3C_2 and NiCr spectra were detected (Fig. 3), with the lower degree of carbide dissolution reflected in the dominant crystalline matrix peak, with a less intense "hump" that was of a higher *d*-spacing relative to the HVOF coating. A striking feature was the lack of visible splat

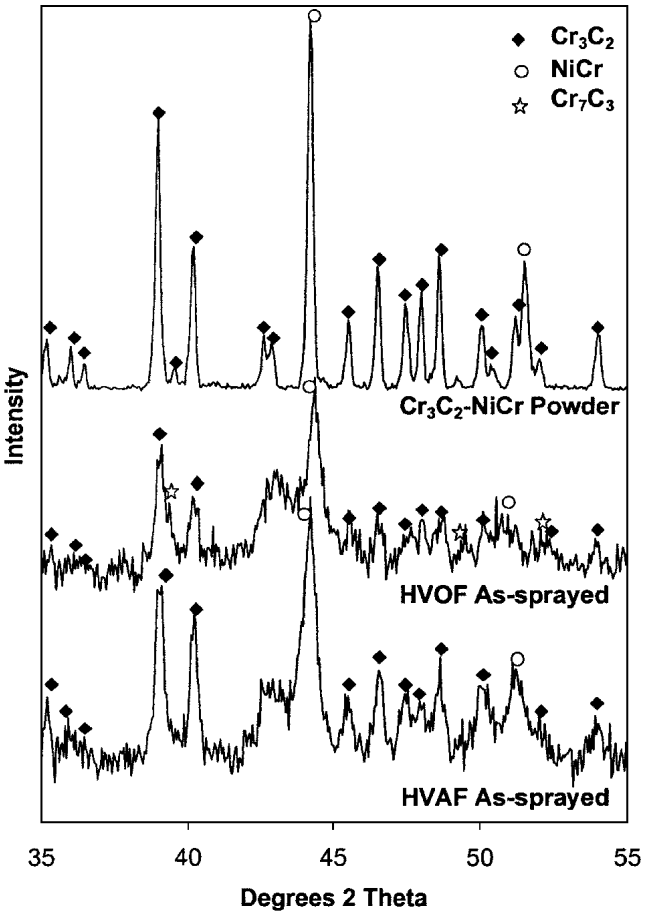

Fig. 3 XRD spectra of the Cr_3C_2-NiCr WOKA 2075NiCr powder and the as-sprayed HVOF and HVAF coatings

structure in this coating. No intersplat oxides were evident, and the lack of widespread carbide dissolution eliminated the matrix-phase contrast of the previous coating.

3.2 Phase Transitions with Heat Treatment

The transformation of the metastable, as-sprayed coating composition occurs rapidly at elevated temperatures (Ref 3, 5, 6, 9, 10, 12). HVOF samples that were treated at 600 and 800 °C for 1 h (Ref 3, 5) showed marked reductions in the amorphous peaks in the XRD spectra, which is indicative of an extensive reduction in the degree of matrix-phase supersaturation. Microstructurally rapid recovery, recrystallization, and grain growth occur as evidenced by the narrowing of the matrix phase peaks. The gray-scale contrast of the as-sprayed coating BSE images was significantly reduced as the reconstitution of the dissolved species occurred through carbide formation (Ref 3-6).

Such transformations were well advanced in the two-day samples. Image analysis of the carbide content (Fig. 4) highlighted the marked reduction in the hard-phase content of the as-sprayed coatings, with that of the HVOF coating significantly more severe than that of the HVAF sample. Extensive carbide recovery occurred within the first two days of treatment, with both coating systems reaching apparently stable concentrations

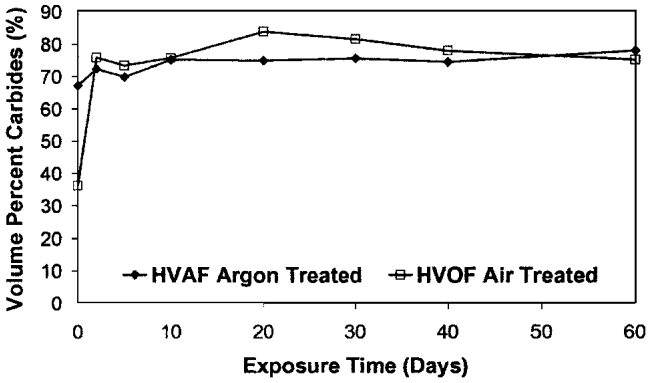

Fig. 4 Variation in the carbide volume fraction of the argon-treated HVAF coatings and the air-treated HVOF coatings as a function of exposure time

of approximately 75 vol.%. The exposure atmosphere had no influence on the rate or long-term magnitude of the carbide recovery. The variations that are evident in Fig. 4 resulted from the nonplanar nature of the BSE images. The analysis volume of the electron beam resolved phases that were slightly below the surface and may have contributed to the larger-than-expected results in some samples.

The XRD of the initial two-day samples were dominated by the NiCr phase, with the amorphous regions of the as-sprayed material no longer apparent beside the narrow, intense peaks (Fig. 5). The carbide peaks were also more defined. The XRD spectra for the long-term trials in air and argon were qualitatively similar to those generated after 2 days. The Cr_2O_3 peaks that were detected were of very low intensity and noisy, suggesting that this compound was present in very low concentrations.

A quantitative analysis was conducted of the XRD spectra to assess the formation of Cr_7C_3 from Cr_3C_2 over extended periods. The XRD peaks were analyzed using the peak area, full width at half-maximum, and center of gravity. The primary Cr_3C_2 peak ($2\theta = 38.5$ to $39.4°$) is overlapped on the lower *d*-spacing side by a secondary Cr_7C_3 peak. This combined peak was compared with an independent secondary Cr_3C_2 peak at $2\theta = 48.3$ to $49.1°$ (the most intense secondary Cr_3C_2 peak was not used due to effects of preferential orientation). This analysis suggested that the HVOF coating had a higher as-sprayed Cr_7C_3 content than the HVAF coating. No significant variation in Cr_7C_3 content was found over the 60 days of heat treatment.

While image analysis of the BSE images indicated no significant increase in carbide content after 2 days, quantitative analysis of the matrix spectra suggested that some degree of carbide formation may have occurred out to 20 days in the argon-treated HVAF coating, and out to 40 days in the HVOF air-treated coating. Figure 6 illustrates the *d*-spacing difference between the center of gravity of the primary NiCr peak ($2\theta = 43.6$ to $44.7°$), and the most intense secondary Cr_3C_2 peak ($2\theta = 39.75$–$40.6°$). (The latter was expected to remain in the same *d*-spacing position irrespective of preferential orientation.) The low concentrations of Cr_7C_3 and Cr_2O_3 meant that their peaks in the vicinity of the matrix spectra would have a negligible influence on the position of the matrix peak. Carbide dissolution during spraying leads to supersaturation of chromium and carbon in the matrix, increasing the average *d*-spacing of the peaks in the matrix XRD

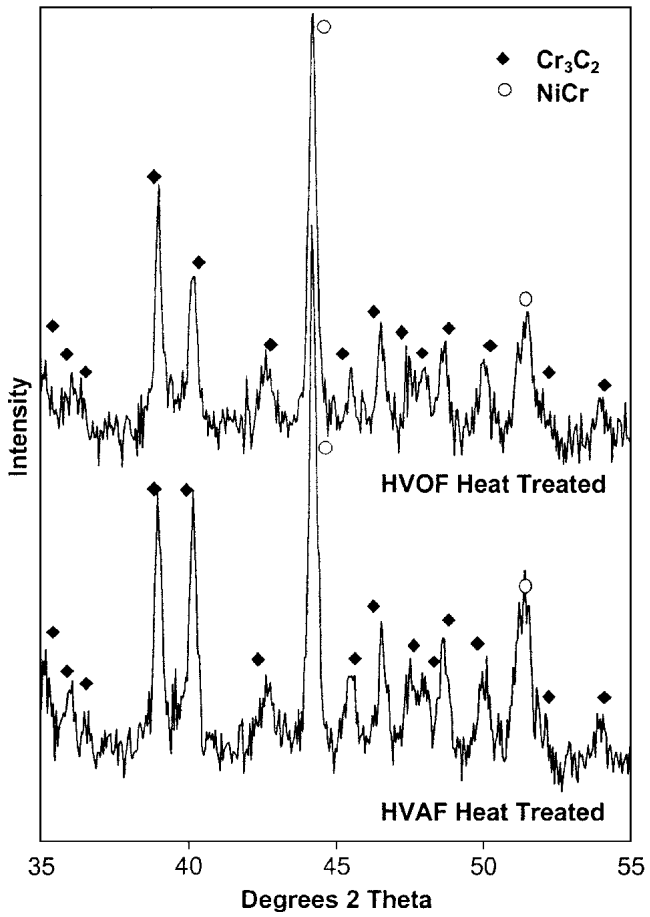

Fig. 5 XRD spectra of the HVOF and HVAF coatings that were heat treated for 2 days at 900 °C

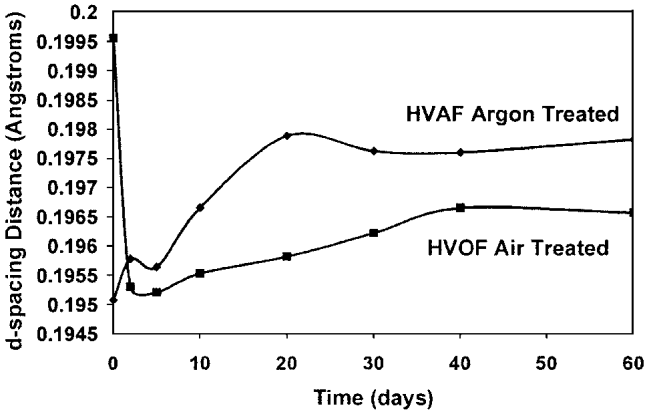

Fig. 6 Variation in the center of gravity *d*-spacing between the primary NiCr peak ($2\theta = 43.6$ to $44.7°$) and the most intense secondary Cr_3C_2 peak ($2\theta = 39.75$ to $40.6°$). The increase in spacing is indicative of a reduction in the degree of chromium and carbon alloying of the matrix phase. The zero time values represent the as-sprayed coatings.

spectra. During heat treatment, the chromium and carbon content of the matrix is reduced, with the *d*-spacing of the matrix peaks decreasing as a result. This caused an increase in the sepa-

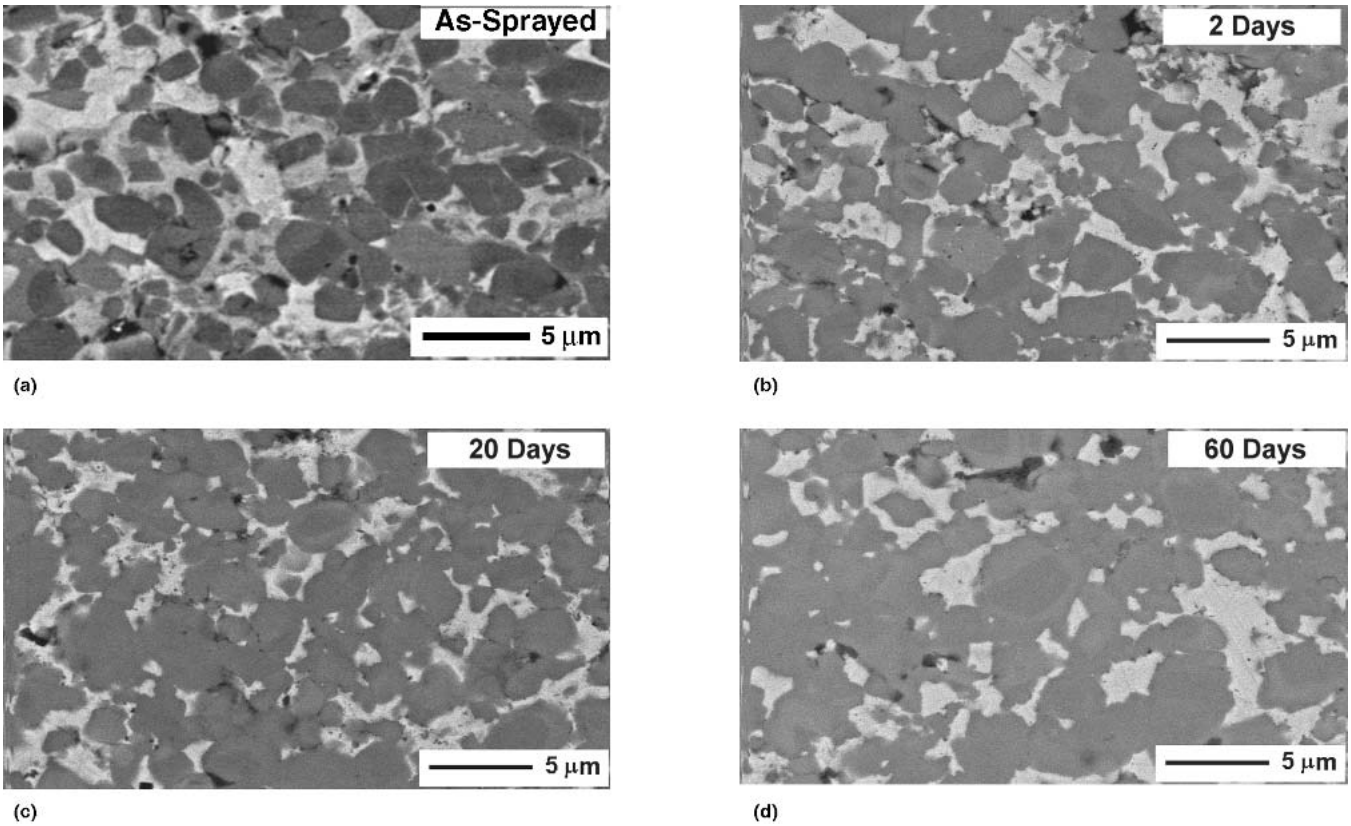

Fig. 7 BSE images of the HVAF microstructure in the (a) as-sprayed condition and after (b) 2, (c) 20, and (d) 60 days of treatment under argon at 900 °C

ration of the Cr_3C_2 and NiCr peaks, which is shown in Fig. 6 for both coatings between 2 and 40 days. The initial decrease in *d*-spacing for the HVOF coating arose from the complication of assessing the center of gravity of the matrix peak in the as-sprayed condition. The 2θ range for the peak analysis was based on the crystalline peaks of the heat-treated spectra. Only the small crystalline peak of the matrix in the as-sprayed coating fell into this range, reflecting a small concentration of relatively unaffected matrix material and not the dominant amorphous material. As such, this peak had a *d*-spacing close to the starting powder, resulting in the large *d*-spacing variation.

Heat treatment of the HVAF coating led to an increase in *d*-spacing separation out to 20 days as a result of a reduction in chromium and carbon content. Beyond this time, a stable peak position was maintained, suggesting that the matrix phase had reached a stable concentration. In contrast, the kinetics of the reduction in matrix phase alloying were significantly slower, taking over 40 days to reach a stable value. This value occurred at a higher *d*-spacing than that for the other system, indicating a higher chromium content. These trends are the opposite of those expected based on the as-sprayed conditions of the two coatings. The as-sprayed HVOF matrix exhibited far greater degrees of chromium and carbon supersaturation than the HVAF coating. A significant driving force would exist for matrix-phase reconstruction and presumably would result in a greater rate of compositional recovery. The reasons behind why the HVOF coating responds so sluggishly and does not attain the same apparent stable peak position as that of the HVAF coating is unknown.

Despite the extended period of high-temperature exposure, the coating compositions did not reach the expected thermodynamic equilibrium predicted using HSC Chemistry software (Ref 17). At 900 °C, the starting powder composition was suggested to reach an equilibrium composition of 41wt.%Cr_3C_2-31wt.%Cr_7C_3-24wt.%Ni-3wt.%Cr-1wt.%C, with negligible $Cr_{23}C_6$ formation. The possible loss of even small amounts of carbon during spraying significantly increased the Cr_7C_3-to-Cr_3C_2 ratio. With a 30 wt.% C loss, a figure approaching the upper limit for most HVOF systems (Ref 3), the Cr_7C_3 content had increased to 54 wt.%. Such high Cr_7C_3 concentrations would be readily apparent in the XRD spectra. The fact that this phase was not definitively observed suggests that the kinetics of carbide transformation are very slow under these conditions. Taylor (Ref 11) came to a similar conclusion from the heat treatment of plasma-sprayed and D-gun-sprayed Cr_3C_2-based coatings.

3.3 Carbide Development with Heat Treatment

3.3.1 HVAF Coating. It is evident from Fig. 7 that the microstructural transformations highlighted in the literature for short-term heat treatments are well advanced after 2 days at 900 °C. The precipitation of fine carbides occurred throughout the coating, primarily in regions of high carbide density. This reflected the low degree of particle heating in-flight as the dissolved chromium and carbon only diffused short distances from the parent carbide grains. Some isolated precipitated carbides

were found. However, the majority had coalesced to form grains with a com-plex morphology. These ranged in shape from thin spidery networks to blocky particles with a "spongelike" appearance that was generated by pockets of trapped matrix phase. Preferential nucleation occurred on those carbides that were retained during spraying. Such peripheral growth of the carbides led to bridging and coalescence, forming larger grains of complex morphology. Of note was the appearance of an additional phase that was present as submicron particles with dark contrast. These were inhomogeneously distributed, appearing at or near the carbide-matrix boundary in regions of high precipitated carbide density. The small size and dark contrast of these particles in the BSE images, particularly in regard to the surrounding high-molecular-weight matrix, suggests that they are of low molecular mass. While such features may be oxides, formed internally by the mechanism proposed by He et al. (Ref 9, 10), they are thought in this work to be carbon particles formed during the reconstitution of the matrix phase. The supersaturated matrix will precipitate carbide grains until the chromium content of the matrix reaches the solubility limit (38 wt.% Cr in nickel at 900 °C) (Ref 25). Once the level of chromium that was dissolved in the matrix drops to this concentration, there is no further concentration-based driving force, leaving more chromium in the matrix than in the original powder. If all of the excess chromium forms Cr_3C_2, as indicated by the XRD analysis, this potentially leaves 13 g of carbon per kilogram of starting material in solution. Because nickel has a very low solubility of carbon at 900 °C (Ref 26), any free carbon must form a separate phase.

Continued carbide growth occurred out to 5 days, with the average carbide size substantially larger than at the shorter time. The reduction in the number of such grains and their more rounded appearance suggests growth via Ostwald ripening (Ref 27). Widespread coalescence and bridging took place with an evident macroscopic carbide skeletal network beginning to form. Beyond 5 days, the development of the carbide structure began to slow. The primary feature of growth was the strengthening of the intercarbide bridging networks and continued carbide coalescence, which led to the development of large single-phase regions of complex shape. The development occurred evenly in all directions around the peripheries of the carbide grains, with no evident preferential growth or distortion of the grain morphology by the splat structure. Within this network, the carbide grains themselves tended to take on more spherical morphologies with extended periods of treatment. Beyond 30 days, no significant changes were evident. The development of the carbide skeletal network had progressed to the point where the carbide phase had become largely continuous, surrounding pockets of matrix phase. The small dark particulate phase was observed out to 60 days, but it did not appear to significantly increase in concentration or undergo coalescence over this period.

The generalized observations from the BSE images were reflected in the quantitative analysis of the average carbide intercept lengths (Fig. 8a). Carbide nucleation led to a decrease in the average carbide size in the HVAF coating. Rapid growth occurred with extended heat treatment out to 20 days, with the rate of increase slowing beyond this point. The reduction in the rate of carbide development is indicative of the increasing significance of a wider carbide skeletal network. While initially the carbides were largely individual entities, continued growth via coalescence and bridging led to a transition from widespread

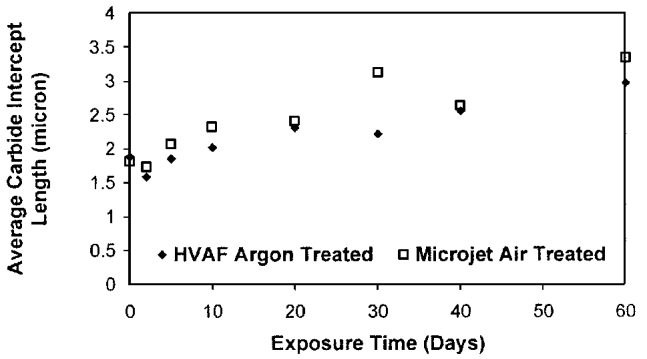

(a)

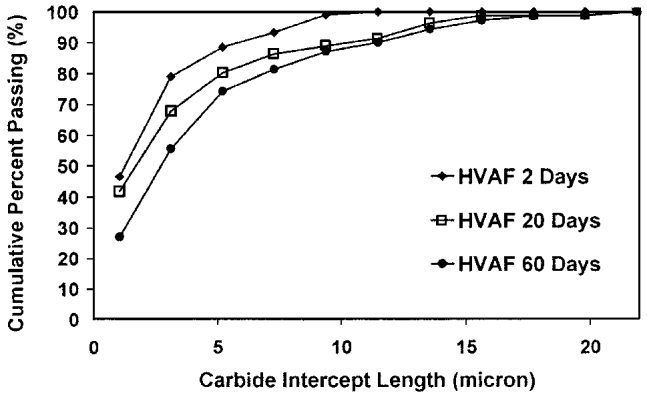

(b)

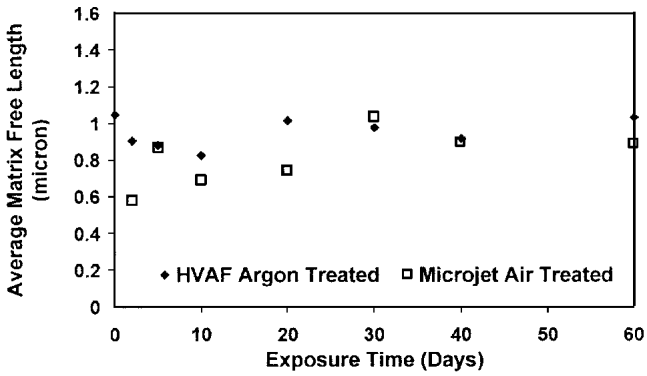

(c)

Fig. 8 (a) The average carbide intercept lengths for the argon-treated HVAF and air-treated HVOF coatings measured at a magnification of 8000×. (b) Cumulative distribution data of the argon-treated HVAF coating illustrating the shift to larger carbide intercept lengths with heat treatment time. (c) The average matrix intercept lengths for the argon-treated HVAF coatings and the air-treated HVOF coatings measured at a magnification of 8000×

particulate reinforcement to the formation of a continuous hard phase. This is more clearly illustrated in the cumulative distribution graphs in Fig. 8(b). At the earliest stages of treatment, a large percentage of the carbides are small, in this case half the measured values falling below 1 μm. With extended exposure, the small size fractions were reduced, with the plots extending out to larger intercept lengths as a result of the carbide skeletal network becoming more defined. The variation in the average

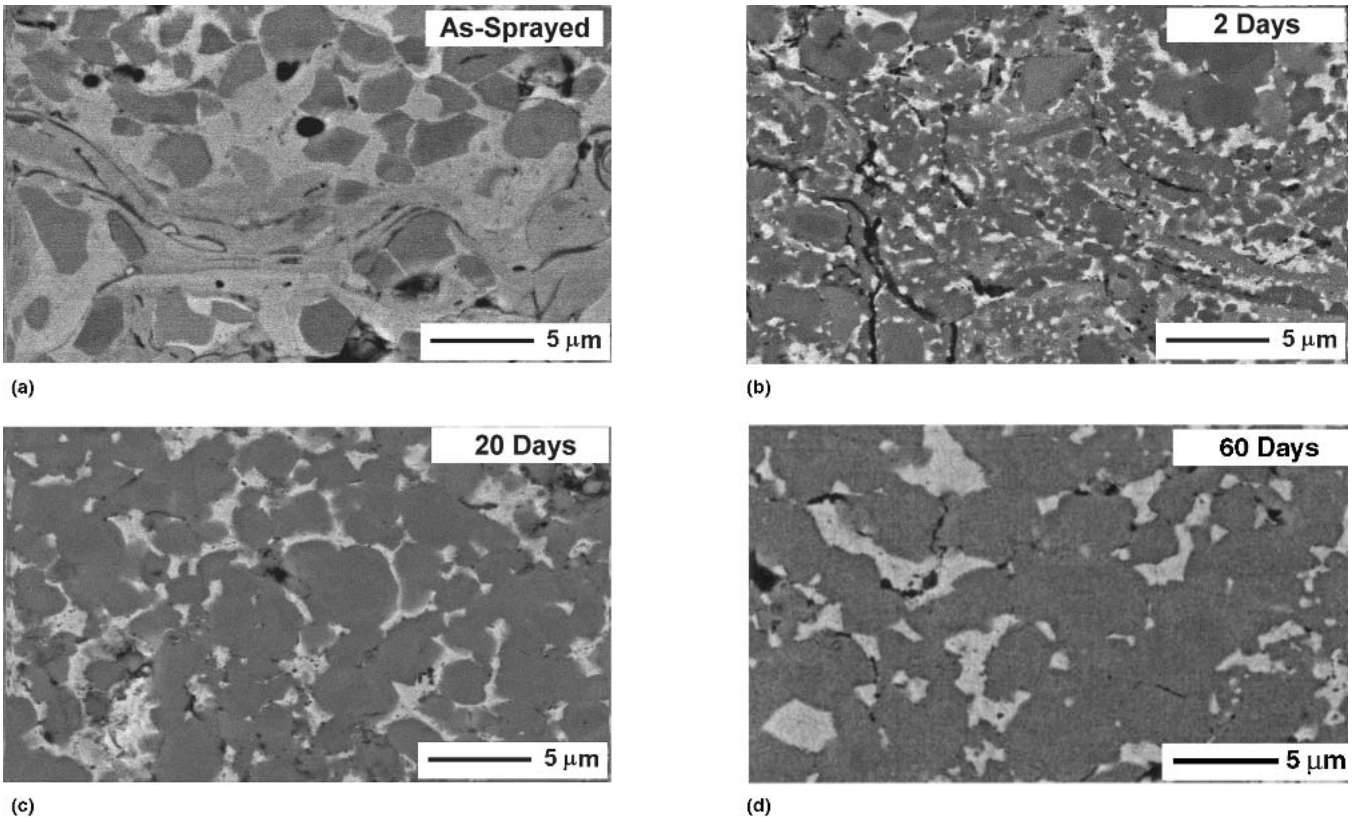

Fig. 9 BSE images of the HVOF microstructure (a) in the as-sprayed condition, and after (b) 2, (c) 20, and (d) 60 days of treatment in air at 900 °C

matrix intercept length was not as definitive as the carbide values (Fig. 8c), with the average length reaching approximately steady values of 0.9 to 1 μm with extended treatment.

Treatment in air led to the same carbide phase transformation with time, as was noted in the argon-treated samples. The dark particulate phase occurred in all samples at a comparable concentration. A subtle difference was in the appearance of oxide phases, which were apparent in a greater concentration than in air. Somewhat unexpectedly, they did not form intersplat oxide stringers, but were noted to occur as small isolated pockets.

3.3.2 HVOF Coating. After 2 days of treatment, the extensive variation in matrix-phase grayscale contrast was significantly reduced, while substantial carbide precipitation occurred (Fig. 9). The nucleated carbides were, on average, smaller than those in the HVAF coating, but were of a much greater concentration. In contrast to the HVAF coating, carbide precipitation took place primarily in carbide-free zones in which the greatest degrees of dissolution had occurred. The variation in the extent of dissolution generated a variety of carbide distributions and morphologies, of which three generalized regions were evident (Fig. 10). Region 1 occurred in the middle of the largest splats in pools of material relatively unaffected by the deposition process. Carbide dissolution was minimal, limiting subsequent carbide precipitation to those areas near the retained carbides in a manner similar to that observed in the HVAF coating. Region 2 occurred midway between the core and the periphery of the largest splats, or in the center of the smaller splats where the matrix had become fully molten in-flight. The retained carbide content was

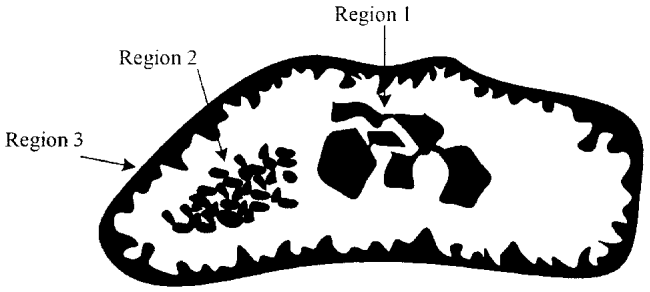

Fig. 10 Schematic illustration of the three generalized regions of carbide development within a splat during heat treatment of the HVOF coating

substantially lower than that in region 1, leading to a highly saturated matrix phase. While some precipitation took place on the retained grains with heat treatment, nucleation occurred primarily within the matrix phase on microstructural features such as dislocations and grain boundaries (Ref 27).

The growth of the highly concentrated fine carbide grains led to the formation of "spongelike" agglomerates. These occupied large areas of the matrix wherever diffusion of the dissolved carbide species had occurred within the softened or largely static molten matrix. While nucleation within such regions appeared to be homogeneous, low-magnification images revealed preferential alignment of the spongy carbide morphologies in relation to the splat structure. Near the center of the splat, such features

appeared equiaxed with only minor degrees of orientation to the splat structure. Near the splat periphery, however, the overall morphology of the carbide clusters became increasingly distorted as a result of the flow of molten supersaturated matrix material upon deposition. The extreme of such carbide alignment occurred in region 3. Occurring at the outer edge of most splats, or within those that had undergone total carbide dissolution, the precipitated carbides in the BSE images appeared to be long, distorted, and thin, which was suggestive of platelike morphologies in three dimensions. At the particle periphery, the temperature is at its highest during spraying. The matrix is likely to be molten, leading to high rates of carbide dissolution and rapid diffusion of the dissolved species. In addition, physical mixing and movement of this layer, both of which lead to the formation of a band of highly concentrated and homogeneously distributed material supersaturated in chromium and carbon, has been proposed (Ref 8). The concentration and distribution of these carbide elements account for the observed carbide morphology during heat treatment. Variation in the powder size is likely to lead to variation in the particle core temperature. The particle core temperature determines the amount of supersaturation of the matrix, which dictates the observed carbide morphology that will be generated following heat treatment.

Growth of the precipitated carbide grains leads to coarsening of the spongy agglomerates, resulting in a more porous appearance. This occurred most rapidly away from the splat boundaries, leading to widespread coalescence and bridging. While the peripheral platelike carbides were still readily evident, after five days they were beginning to break up into more isolated grains. After 10 to 20 days, the structure had developed to a state that was comparable to that of the HVAF coating. Growth and spheroidization of the individual grains was evident, leading to widespread bridging and to the development of an expansive skeletal network. Such macroscopic development began to overshadow the preferential orientation of the carbides in relation to the splat shape. Beyond 30 days, carbide growth slowed in a manner similar to that of the HVAF coating. By 60 days, the HVOF and HVAF coating microstructures were comparable, although the carbides in the HVOF coating showed a wider distribution in size and more complex distorted morphologies relative to the spherical grains in the HVAF coating. It was evident, however, that, despite the marked variation in the as-sprayed condition, both coating systems tended toward the same microstructure of coalesced, spherical carbide grains, each with a diameter of approximately 2.5 μm.

The apparent anomaly in trends of the quantitative HVOF carbide intercept analysis (Fig. 8a) and the BSE imaging arises from the fine scale of the precipitated carbides. At a magnification of 8000×, the nucleated carbides were not resolvable as separate entities. Instead, the spongy agglomerates appeared as larger midgray carbides, accounting for the apparently larger average intercept length of the HVOF system. The actual intercept length is expected to be significantly lower than illustrated, considering the high concentration of small carbides that is evident in the higher magnification images. Rapid growth occurred out to 20 days, beyond which the rate of growth slowed, with intercept lengths that were similar to those of the HVAF coating. The greater initial carbide growth rate in the HVOF coatings in Fig. 8(a) is thought to reflect the differing mechanisms of development between the two coatings. In the HVAF coating, a limited

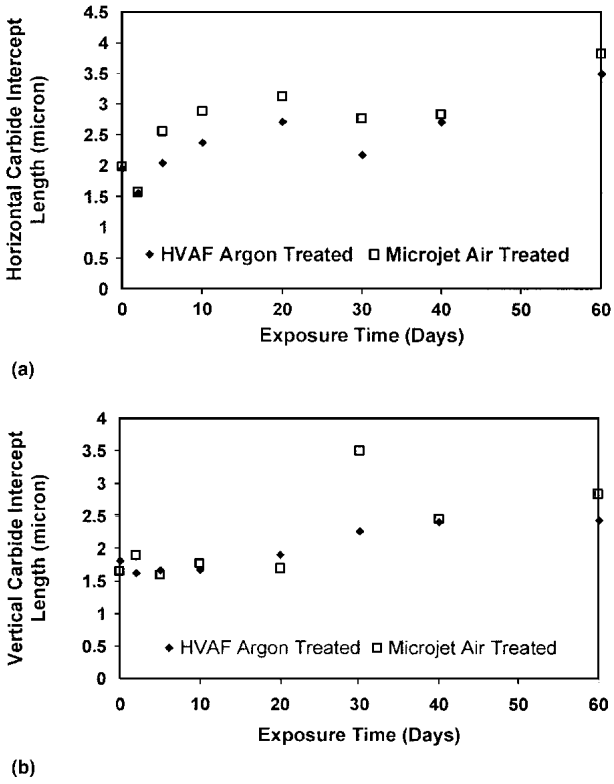

Fig. 11 (a) Horizontal carbide intercept lengths of the argon-treated HVAF and the air-treated HVOF coatings measured at a magnification of 8000×. (b) Vertical carbide intercept lengths of the argon-treated HVAF and the air-treated HVOF coatings measured at a magnification of 8000×

degree of carbide precipitation occurred and was associatedprimarily with the high concentration of retained carbides. As such, the intercept lengths were primarily in relation to the relatively stable retained carbide content, with the smaller values related to the small spurs and bridges generated by the preferential nucleation of new grains on their surface. In contrast, the HVOF carbide intercept lengths were predominantly generated by the growth of the expansive carbide agglomerates, rather than individual nucleated grains. The large driving force for microstructural development resulting from the high interfacial area of such features accounts for the greater rate of development and the greater magnitude of carbide intercept lengths relative to the HVAF samples. This is in contrast with the higher-magnification BSE images, which showed that, while the carbide growth was very rapid in the HVOF coating, the average carbide dimensions were greater in the HVAF coating.

The growth of the nucleated carbides occurred in a heterogeneous manner throughout the coatings, with the preferential orientation along the splat axis particularly marked in the HVOF coatings. Figure 11 illustrates the horizontal (Fig. 11a) and vertical (Fig. 11b) carbide intercept lengths for both coating types. In the as-sprayed condition, both coatings showed a slight preferential horizontal orientation. Carbide nucleation with heat treatment reduced the average horizontal intercept length in both coatings, with the average value of the HVOF coating expected to be substantially smaller than that illustrated. Extended treat-

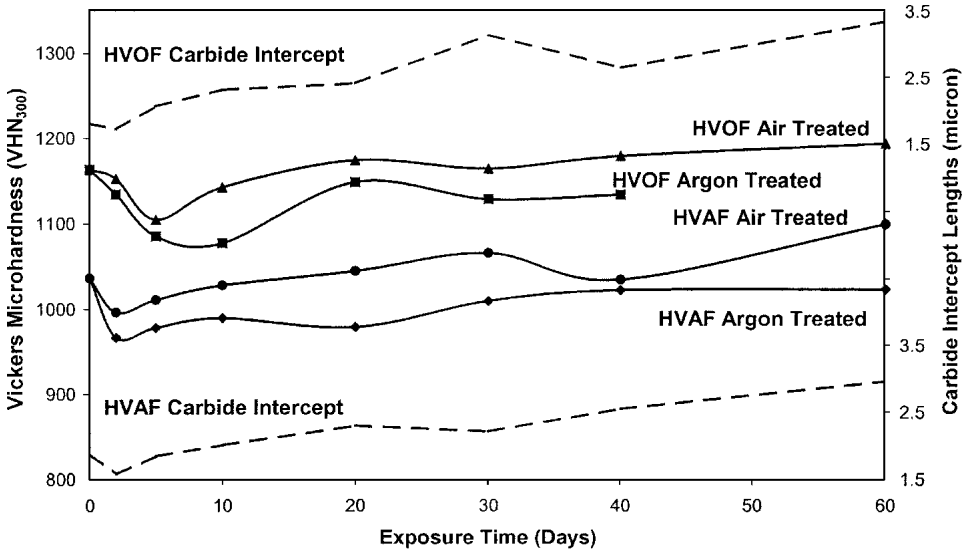

Fig. 12 Vickers microhardness results for the HVAF and HVOF coatings. The 60 day HVOF specimen treated in argon was too thin for microhardness testing. Overlaid are the carbide intercept results for both coatings based on the high-magnification (8000×) data (dotted lines).

ment led to rapid growth in this direction in the HVOF coatings, reaching a plateau of approximately 2.7 to 3 μm after 10 days. The HVAF coating exhibited a much slower rate of growth, taking 20 days to reach a similar intercept length.

In the vertical direction, carbide growth was slower, showing only a slight increase over the first 20 days for both coatings. Growth after this period was more rapid, with values of 2.5 to 2.75 μm achieved in all cases. Significantly, such results indicate preferential growth in the horizontal direction during the early stages of carbide development for both coating systems, a point not readily apparent in the BSE images of the HVAF coating. This trend confirms that observed in the BSE images of the HVOF coatings. The long-term response of the horizontal and vertical intercept lengths toward the same value correlates with the spheroidization of the carbide structure that is evident in the BSE images. This was particularly apparent in the HVAF coatings, in which the coalesced grains themselves tended toward a spherical morphology. The transition in this period in which the average carbide intercept length remained approximately stable may have reflected a transition in mechanism in the minimization of interphase surface area. Initially, this is likely to be driven by the high concentration of small isolated or agglomerated carbide grains. Beyond 20 days, however, the concentration of such small particles was negligible, with further reductions in interfacial area thought to result from the spheroidization of the existing carbide morphology.

Treatment in air had no obvious influence on the carbide nucleation or growth processes. The presence of oxide in the as-sprayed coating complicated the assessment of oxide ingress. However, the pockets of oxide and thickening of the oxide stringers appeared more frequently in the air-treated samples. The thinner nature of these samples, combined with the high splat surface area per depth of coating generated by the splat morphology, suggested that such internal oxidation would be more extensive in these coatings than in the HVAF samples.

3.4 Coating Microhardness

While the HVOF coatings exhibited consistently higher hardness readings, both coating systems followed the same trend with heat treatment in air and argon (Fig. 12). Initially, the hardness dropped with heat treatment, with the magnitude of softening most dramatic in the HVOF coatings. Hardness recovery occurred rapidly with additional heat treatment, again being most significant in the HVOF coatings. The rate of hardness increase slowed with time in both coatings, with stable values achieved after 20 to 30 days.

An analysis of the various hardening mechanisms as a function of time is the focus of current work. The key findings are reviewed here to correlate the observed trends with the results of this analysis. In the as-sprayed condition, an extremely complex condition exists in both coating systems. The contribution of the hard carbide phase initially is dictated more by concentration than by morphology. As such, the higher retained carbide content of the HVAF coating would be expected to generate higher hardness values than those for the HVOF coating. This was not observed, however, indicating that other hardening mechanisms were operative. Hardening of the matrix is one of these, particularly the solid solution strengthening generated by the extensive degree of carbide dissolution.

The marked softening of both the HVAF and HVOF coatings with heat treatment is thought to have resulted from the reduction in mechanisms of matrix-phase strengthening. The lower retained carbide content of the HVOF coating is thought to have contributed to the greater magnitude of hardness loss relative to the HVAF coatings. Carbide development is believed to account for the rapid increase in hardness over the period of 2 to 10 days. The initial recovery is thought to have been dictated primarily by the variation in carbide development on a fine scale. In the HVAF coating, the high-magnification (8000×) carbide intercept results followed the same trend as the hardness data, highlighting the dependence on the carbide development. This cor-

relation in the HVOF coatings is not as distinct due to the variation in the mechanism of carbide development. The preferential nucleation of carbides on and around the retained grains in the HVAF coating meant that the development of a wider carbide network was developed early on, leading to an increase in hardness. In contrast, the HVOF carbides developed as relatively independent agglomerates. While the features of small carbide size and fine matrix-free lengths within such features would suggest that, as an entity, they act as additional hard-phase particles (Ref 21, 28, 29), it is not until more widespread carbide interaction occurs that the hardness begins to increase.

Beyond 20 to 30 days, the microstructures of both coatings were comparable, as were the trends in microhardness. In this period, the emphasis shifted from the individual carbide attributes to those of the widespread carbide skeletal structure. While additional hardening mechanisms relating to the physical splat structure are likely to contribute, these results suggested that after 2 to 5 days of matrix-phase transformation the long-term response of Cr_3C_2-NiCr HVAF and HVOF coatings is critically dependent on the mechanism and rate of carbide-phase development.

3.5 Implications for Long-Term Exposure

While several trends have been highlighted in this work contrasting the rate and mechanism of carbide development, the most significant trend over all the data is the similarity in the responses of both coatings during the latter stages of treatment. The as-sprayed condition of the HVAF and HVOF coatings differed greatly in both composition and microstructure, yet after 60 days of treatment the compositions of the matrix and carbide phases were comparable. In addition, the carbide morphology showed the same trends in growth, preferential orientation, spheroidization, and magnitude of intercept length.

It must be emphasized, however, that these trials were conducted at 900 °C, the upper limit of the operating range of 850 to 900 °C that is typically specified by powder manufacturers. While the same general microstructural developments are expected to occur at lower temperatures based on the images presented in previous works (Ref 3-6, 9, 10), the rate at which such features develop relative to those observed here will be slower. It is likely that the initial transitions of carbide nucleation and growth occur very quickly across the range of operating temperatures for high-velocity sprayed Cr_3C_2-NiCr coatings due to the large compositional driving force. Subsequent carbide development, however, is thought to be dictated primarily by the diffusion of chromium and carbon. The diffusion of chromium is likely to be relatively slow, even at high temperatures, due to its substitutional position in the nickel matrix. However, the high solubility of chromium in this phase reduces the amount of this element that must diffuse to any point to form the carbide phase. Carbon diffusion would be expected to have a high rate of diffusion through interstitial sites in the lattice. However, the low solubility of carbon in the matrix may mean that these atoms have to diffuse the greatest distance to enable sufficient concentrations to be achieved for carbide formation. Should the diffusion of carbon be the rate-limiting step, then calculation of the relative diffusivities at lower temperatures for carbon in nickel suggests that it will take four times as long at 800 °C and 20 times as long at 700 °C to form microstructures comparable to those observed here at each time period. Should chromium diffusion be rate controlling, then the time for comparable structure formation would be significantly longer. Hence, while the initial rates of microstructural refinement are likely to be comparable, subsequent diffusion-controlled carbide growth is likely to take substantially longer at lower temperatures. As such, any microstructure-influenced properties of the coatings would be expected to vary extensively over the life of the coating. Such variation would be expected to be more prominent in the HVOF coating considering the extensive amount of carbide reinforcement and growth required to achieve the same overall morphology as that evident in the HVAF coatings.

4. Conclusions

In this work, the microstructural transformations of HVAF and HVOF Cr_3C_2-NiCr coatings were assessed following heat treatment at 900 °C for a period of up to 60 days in air and argon. The key findings from this analysis were:

- Carbide dissolution during spraying occurred to a significantly greater extent in the HVOF coating than in the HVAF coating.
- Compositional recovery occurred rapidly, with a relatively stable composition reached within 2 days. Minor compositional changes in the matrix continued out to 40 days of treatment at 900 °C.
- Cr_3C_2 did not significantly degrade to Cr_7C_3 within the coating with long-term exposure. This was in contrast to the expected thermodynamic equilibrium composition, indicating that the metastable composition showed very slow kinetics toward equilibrium.
- The mechanism of carbide growth varied between the HVAF and HVOF coatings, dictated by the extent of carbide dissolution during spraying. The minimal dissolution in the HVAF coatings meant that growth was associated on and around the retained carbides. In the HVOF coatings, carbide development occurred mainly through the agglomeration of nucleated carbides in regions of significant carbide dissolution.
- Treatment in air and argon resulted in the same mechanisms and rate of carbide nucleation and growth.
- Preferential horizontal carbide growth occurred in both coating systems over the first 20 to 30 days. The development of a widespread carbide skeletal network and the general spheroidization of the carbide morphology led to more equiaxed dimensions with extended exposure.
- Despite the marked variation in the as-sprayed condition, the HVAF and HVOF coatings tended toward the same composition, carbide size, and morphology after 30 to 40 days of treatment at 900 °C.
- The development of the carbide network had a significant role in the variation in microhardness with heat treatment.

Acknowledgment

The authors gratefully acknowledge the assistance of WOKA, Metal Spray Suppliers (New Zealand) Ltd., and Holster Engineering (New Zealand) Ltd. for supplying the powder and

coatings for this work. The financial assistance provided by Material Performance Technologies (New Zealand) and The University of Auckland is greatly appreciated.

References

1. P. Sahoo and R. Raghuraman, Chromium Carbide Reinforced Composite Coatings for High Temperature Hard-Coat Applications, *Thermal Spray: Research, Design and Applications,* C.C. Berndt and T.F. Bernecki, Ed., June 7-11, 1993 (Anaheim, CA), ASM International, 1993, p 405-410
2. P. Sahoo and R. Raghuraman, High Temperature Chromium Carbide Reinforced Metal Matrix Composite Coatings for Turbomachinery Applications, *TS93: Thermal Spraying Conference (Thermische Spritzkonferenz),* Deutscher Verlag fur Schweisstechnik DVS-Verlag GmbH, 1993, p 296-300
3. S. Zimmermann and H. Kreye, Chromium Carbide Coatings Produced with Various HVOF Spray Systems, *Thermal Spray: Practical Solutions for Engineering Problems,* C.C. Berndt, Ed., Oct 7-11, 1996 (Cincinnati, OH), ASM International, 1996, p 147-152
4. T. Tomita, Y. Takatani, K. Tani, and Y. Harada, Mechanisms of High Hardness in Cr_3C_2-NiCr Cermet Coatings Formed by Vacuum Plasma Spraying, *Thermal Spray 2001: New Surfaces for a New Millennium,* C.C. Berndt, K.A. Khor, and E.F. Lugscheider, Ed., May 28-30, 2001 (Singapore), ASM International, 2001, p 699-704
5. F. Otsubo, H. Era, T. Uchida, and K. Kishitake, Properties of Cr_3C_2-NiCr Cermet Coating Sprayed by High Power Plasma and High Velocity Oxy-Fuel Processes, *J. Thermal Spray Technol.,* Vol 9 (No. 4), 2000, p 499-504
6. J.M. Guilemany, J. Nutting, and N. Llorca-Isern, Microstructural Examination of HVOF Chromium Carbide Coatings for High Temperature Applications, *J. Thermal Spray Technol.,* Vol 5 (No. 4), 1996, p 483-489
7. J.M. Guilemany and J.A. Calero, Structural Characterization of Chromium Carbide-Nickel Chromium Coatings Obtained by HVOF-Spraying, *Thermal Spray: A United Forum for Scientific and Technological Advances,* C.C. Berndt, Ed., Sept 15-18, 1997 (Indianapolis, IN), ASM International, 1997, p 717-721
8. V.V. Sobolev and J.M. Guilemany, Effect of Oxidation on Droplet Flattening and Splat-Substrate Interaction in Thermal Spraying, *J. Thermal Spray Technol.,* Vol 8 (No. 4), 1999, p 523-530
9. J. He, M. Ice, J. Schoenurg, D. Shin, and E. Lavernia, Thermal Stability of Nanostructured Cr_3C_2-NiCr Coatings, *J. Thermal Spray Technol.,* Vol 10 (No. 2), 2001, p 293-300
10. J. He and E.J. Lavernia, Precipitation Phenomenon in Nanostructured Cr_3C_2-NiCr Coatings, *Mater. Sci. Eng., A,* Vol 301, 2001, p 69-79
11. T.A. Taylor, Phase Stability of Chrome-Carbide Ni-Cr Coatings in Low Oxygen Environments. *J. Vac. Sci. Technol.,* Vol 12 (No. 4), 1975, p 790-794
12. I. Fagoaga, J.L. Viviente, P. Gavin, J.M. Bronte, J. Garcia, and J.A. Tagle, Multilayer Coatings by Continuous Detonation System Spray Technique, *Thin Solid Films,* Vol 317, 1998, p 259-265
13. D.R. Sielski and P. Sahoo, Chromium Carbide Coatings for High Temperature Erosion Resistance, *Thermal Spray: Practical Solutions for Engineering Problems,* C.C. Berndt, Ed., Oct 7-11, 1996 (Cincinnati, OH), ASM International, 1996, p 159-167
14. B.Q. Wang and K. Luer, The Relative Erosion-Corrosion Resistance of Commercial Thermal Sprayed Coatings in a Simulated Circulating Fluidized Bed Combustor Environment, *Thermal Spray Industrial Applications,* C.C. Berndt and S. Sampath, Ed., June 20-24, 1994 (Boston, MA), ASM International, 1994, p 115-120
15. B.Q. Wang, Erosion-Corrosion of Coatings by Biomass-Fired Boiler Fly Ash, *Wear,* Vol 188, 1995, p 40-48
16. S. Tobe, Y. Andoh, K. Hidaka, K. Tanaka, S. Nishimura, K. Kawaharada, and H.K. Shirai, High Temperature Corrosion Resistance of Newly Developed Cr-Based Alloy Coatings, *Tagungsband Conference Proceedings,* E. Lugscheider and R.A. Kammer, Ed., DVS Verlag GmbH, 1999, p 296-300
17. A. Roine, *HSC Chemistry*, Outokumpo Research, Oy, Finland, 1997
18. D. Wilcox, B. Dove, D. McDavid, and D. Greer, *UTHSCSA Image Tool for Windows,* The University of Texas Health Research Center, 1995
19. F.B. Pickering, *The Basis of Quantitative Metallography,* Institute of Metallurgical Technicians, London, U.K., 1976
20. E.E. Underwood, Applications of Quantitative Metallography, *Metallography, Structures and Phase Diagrams,* T. Lyman, Ed., American Society for Metals, 1973, p 37-47
21. J. Gurland, Application of Quantitative Microscopy to Cemented Carbides, *Practical Applications of Quantitative Metallography,* J.L. McCall and J.H Steele, Jr., Ed., American Society for Testing and Materials, 1984, p 65-84
22. K. Akimoto and Y. Horie, Study of HVAF WC-Cermet Coatings, *Thermal Spraying: Current Status and Future Trends,* A. Ohmori, Ed., High Temperature Society of Japan, 1995, p 313-316
23. L. Jacobs, M.M. Hyland, and M.D. Bonte, Comparative Study of WC-Cermet Coatings Sprayed Via the HVOF and HVAF Processes. *J. Thermal Spray Technol.,* Vol 7 (No. 2), 1998, p 213-218
24. L. Jacobs, M.M. Hyland, and M.D. Bonte, Study of the Influence of Microstructural Properties on the Sliding-Wear Behavior of HVOF and HVAF Sprayed WC-Cermet Coatings, *J. Thermal Spray Technol.,* Vol 8 (No. 1), 1999, p 125-132
25. P. Nash, Cr-Ni Phase Diagram, *Binary Alloy Phase Diagrams,* T.B. Massalski, Ed., ASM International, 1992, p 1298-1301
26. M. Singleton and P. Nash, C-Ni Phase Diagram, *Binary Alloy Phase Diagrams,* T.B. Massalski, Ed., ASM International, 1992, p 866-867
27. J.W. Martin, *Micromechanisms in Particle-Hardened Alloys,* Cambridge Solid State Series, R.W. Cahn, M.W. Thompson, and I.M. Ward, Ed., Cambridge University Press, 1980
28. H.C. Lee and J. Gurland, Hardness and Deformation of Cemented Tungsten Carbide, *Mater. Sci. Eng.,* Vol 33, 1978, p 125-133
29. H. Engqvist, S. Jacobson, and N. Axen, A Model for the Hardness of Cemented Carbides *Wear,* Vol 252, 2002, p 384-393